

Multiterminal transport spectroscopy of subgap states in Coulomb-blockaded superconductorsRubén Seoane Souto ^{1,2}, Matteo M. Wauters ^{1,3}, Karsten Flensberg ¹, Martin Leijnse^{1,2} and Michele Burrello^{1,3}¹*Center for Quantum Devices, Niels Bohr Institute, University of Copenhagen, 2100 Copenhagen, Denmark*²*Division of Solid State Physics and NanoLund, Lund University, S-22100 Lund, Sweden*³*Niels Bohr International Academy, Niels Bohr Institute, University of Copenhagen, 2100 Copenhagen, Denmark*

(Received 7 September 2022; accepted 13 December 2022; published 22 December 2022)

Subgap states are responsible for the low-bias transport features of hybrid superconducting-semiconducting devices. Here we analyze the local and nonlocal differential conductance of Coulomb-blockaded multiterminal superconducting islands that host subgap states with different spatial structures. The emerging patterns of their transport spectroscopy are used to characterize the possible topological nature of these devices and offer the possibility of controlling their transport properties. We develop a next-to-leading order master equation to describe the multiterminal transport in superconductors with both strong Coulomb interactions and multiple subgap states, coupled with metallic leads. We show that the nonlocal differential conductance characterizes the spatial extension of the subgap states and signals the presence of degenerate bound states with a finite support on different parts of the device. Additionally, it displays sharp sign changes as a function of the induced charge of the superconductor, signaling energy crossings among its lowest excited states.

DOI: [10.1103/PhysRevB.106.235425](https://doi.org/10.1103/PhysRevB.106.235425)**I. INTRODUCTION**

Hybrid systems fabricated with superconducting and semiconducting materials are considered a key ingredient for the development of quantum technologies and have demonstrated a potential for quantum information storage and processing [1–4]. In particular, the advent of topological superconductors has raised the hope of realizing protected quantum devices, robust to decoherence induced by local perturbations [5].

In one dimension, topological superconductors host Majorana subgap modes [6], predicted to be non-Abelian anyons and to give rise to several nonlocal properties [7–10]. These Majorana modes are exponentially localized at the system edges but, importantly, each pair of them defines a nonlocal quasiparticle state, with vanishing energy in the ideal case. In this context, distinguishing between local and nonlocal subgap states becomes relevant for identifying devices that are potentially in the topological regime.

Subgap states dominate the transport properties of superconducting devices at low voltage bias and they can be experimentally detected with tunneling spectroscopy. In particular, zero-energy Majorana modes in grounded topological superconductors reveal themselves through a quantized conductance peak at zero bias [11–14]. However, also trivial states can mimic similar transport features in local spec-

troscopy, see for example Refs. [15–24]. This motivated further analyses of the nonlocal conductance in multiterminal setups, where the device couples to a grounded superconductor [25–32], with experiments performed in nanowires [33–38], and devices based on two-dimensional electron gases [39–42].

When the superconductor is not grounded but exhibits a strong charging energy, the intricate interplay between superconductivity and many-body interactions yields a rich phenomenology. In the topological regime, Coulomb-blockade effects provide effective tools to initialize, read out, and measure coherence times in topological qubits, thus constituting a key element to design platforms for quantum information devices [43–53].

Transport properties of floating superconducting islands have been extensively studied experimentally in semiconducting nanowires, with the goal of extracting quasiparticle poisoning times [54,55], showing the doubling of Coulomb peaks in the high-field regime [56–59], and investigating the exponential protection [56] and spin polarization [60] of subgap states. These systems have been explored using interferometry [61] and reflectometry techniques [62,63]. However, most of the studies so far, both experimental and theoretical, focused on local conductance measurements of two-terminal devices; nonlocal transport properties of multiterminal Coulomb-blockaded devices remain largely unexplored.

A more complex typology of devices is based on two nanowires coupled via a floating superconductor, sharing a common charging energy. In the case where the device couples to more than two leads, the topological Kondo effect is predicted to appear, and its realization would be an unequivocal signature of the Majorana nonlocality [64–66]. As such, systems with Coulomb-blockaded double nanowires are at the

Published by the American Physical Society under the terms of the [Creative Commons Attribution 4.0 International](https://creativecommons.org/licenses/by/4.0/) license. Further distribution of this work must maintain attribution to the author(s) and the published article's title, journal citation, and DOI. Funded by [Bibsam](https://www.bibsam.com/).

focus of recent experiments [67,68] and theoretical investigations [69].

In this work we propose multiterminal quantum transport measurements as a way to distinguish between local and nonlocal subgap states in Coulomb-blockaded superconducting devices. We focus on two geometries, namely a single and a double superconducting nanowire device. We employ a second-order master equation approach that allows for studying both sequential and cotunneling transport in superconducting devices with strong Coulomb interaction, multiple subgap states, and the coupling to two or more metallic leads. In particular, we show that sequential transport at low bias voltages is blocked whenever the lowest-energy subgap state does not couple two of the leads. Indeed, even though the Coulomb interaction is highly nonlocal, transport is dominated by the local projection of subgap states, providing indications about their spatial structure. Moreover, a three-terminal Coulomb-blockaded device displays abrupt changes in the current direction at fixed bias potential as a function of the charge n_g induced on the superconducting island, due to energy crossings in the excitation spectrum, similarly to nonsuperconducting Coulomb-blockaded quantum dots [70]. Concerning the double nanowire geometry, we investigate the local and nonlocal conductance associated with different spatial structures of the subgap states, aiming to facilitate the interpretation of future experiments.

The rest of the paper is organized as follows. In Sec. II we present the effective zero bandwidth model we use to describe the low-energy behavior of the devices and the formalism used to compute the sequential and cotunneling current signals. In Sec. III we investigate both the two-terminal and three-terminal conductance of a single nanowire with one or multiple subgap states. In Sec. IV we analyze the transport signatures associated with different structures of the subgap states in the double nanowire geometry. We draw our conclusions and discuss future developments in Sec. V. The Appendixes contain more supporting results and a detailed derivation of the tunneling rates calculation.

II. MODEL AND METHODS

We consider a superconducting island coupled to normal metallic electrodes, given by the Hamiltonian

$$H = H_L + H_I + H_T, \quad (1)$$

where the leads are described by

$$H_L = \sum_{\nu, k, \sigma} (\xi_{\nu k \sigma} - \mu_\nu) c_{\nu k \sigma}^\dagger c_{\nu k \sigma}, \quad (2)$$

with the electron energy $\xi_{\nu k \sigma}$ and the annihilation operator $c_{\nu k \sigma}$ referring to an electron in lead ν with momentum k and spin $\sigma \in \{\uparrow, \downarrow\}$. We assume that each lead remains in internal equilibrium, described by a Fermi-Dirac distribution n_F with chemical potential μ_ν and temperature T .

The superconducting island is described by

$$H_I = \sum_{j, \sigma} \varepsilon_{j \sigma} \gamma_{j \sigma}^\dagger \gamma_{j \sigma} + E_{\text{el}}(N), \quad (3)$$

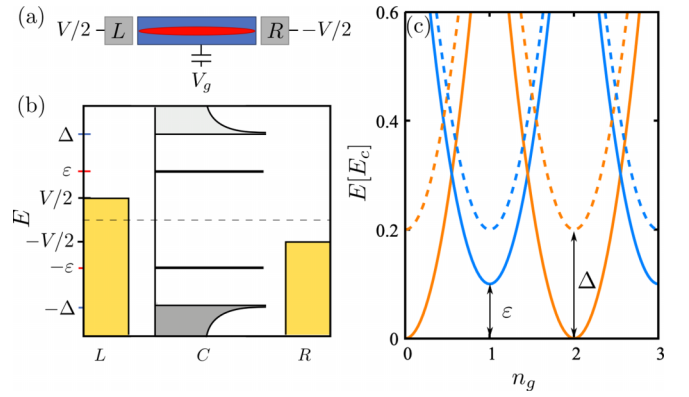


FIG. 1. (a) Sketch of a Coulomb-blockaded hybrid superconducting nanowire device, hosting a subgap state (red). In this example, the nanowire couples to two leads (indicated with L and R). (b) Single-particle energies of the island, containing a subgap state at energy ε (black line), quasiparticle excitations above the gap Δ , and the lead states displaying Fermi-Dirac distributions (yellow) at different chemical potentials. (c) Lowest eigenenergies in the presence of interactions as a function of the offset charge $n_g = \alpha V_g$ with α being the lever arm. Blue (orange) lines correspond to states with an odd (even) number of electrons in the island. We show an example where the nanowire hosts a spinless subgap state, where the solid and dashed lines correspond to the ground state and the excited state in each charge sector.

where j labels a state with energy $\varepsilon_{j \sigma}$, and the Bogoliubov–de Gennes (BdG) operators read

$$\gamma_{j \sigma} = u_j d_{j \sigma} - \rho_\sigma v_j e^{-i\phi} a_{j \bar{\sigma}}^\dagger. \quad (4)$$

Here d and d^\dagger are annihilation and creation operators of electrons in the island, u_j and v_j are the BdG coefficients for the subgap states, ϕ is the superconducting phase operator, such that $e^{-i\phi}$ annihilates a Cooper pair in the island, and $\rho_\sigma = \pm$ for $\sigma = \uparrow, \downarrow$.

The electrostatic repulsion term is given by

$$E_{\text{el}}(N) = E_C(N - n_g)^2, \quad (5)$$

where n_g is the dimensionless gate-induced charge offset and N is the (excess) electron number operator, accounting for the fermionic occupation of the states and the number of Cooper pairs on the island. Figure 1(a) sketches the device described by this model, in the case of only two leads and a single nanowire. Figures 1(b) and 1(c) represent the superconducting quasiparticle spectrum and the many-body energy levels, respectively.

Finally, the tunneling between leads and the superconducting island is described by the Hamiltonian

$$H_T = \sum_{\nu, k, j, \sigma} (t_{\nu k \sigma} c_{\nu k \sigma}^\dagger d_{j \sigma} + \text{H.c.}), \quad (6)$$

where t is the tunneling amplitude. The corresponding tunneling rates are defined as $\Gamma_{\nu, j, \sigma} = 2\pi \rho_{F\nu} |t_{\nu, j, \sigma}|^2$, and we consider them k independent (wide-band limit), where $\rho_{F\nu}$ is the density of states at the Fermi level of the lead ν .

In this work we employ a zero-bandwidth approximation for the superconducting island, meaning that we consider only two relevant energy levels $\varepsilon_{0, \uparrow} = \varepsilon$ and $\varepsilon_{1, \sigma} = \Delta > \varepsilon$.

The first represents a low-energy spin-polarized subgap state whose spatial structure and degeneracy will be the main focus of our work. The state at energy Δ is a spin-degenerate level and represents an effective description of the proximitized superconducting continuum which extends through the whole hybrid device. This approximation models a short nanowire where the quasiparticle spectrum above the proximity induced superconducting gap displays a quantization determined by the finite system size. The corresponding lowest energy excitation can mediate elastic cotunneling processes through the device. A possible alternative is to consider a number of degenerate states at energy Δ , each coupled to a single lead. Each of these states models a metallic quasiparticle continuum with a strong relaxation towards the bottom of the continuum band. With this choice, the states at energy Δ cannot mediate elastic cotunneling transport. Throughout the rest of the paper we focus on the first scenario, where each nanowire hosts a single extended superconducting continuum, to avoid an excessive increase of the computational run time. However, this choice does not qualitatively influence the transport features at low bias, where the conductance is dominated by the subgap states. See Fig. 6 in Appendix B for a comparison of the two cases.

A. Formalism

In this work we focus on the regime where $\Gamma_{\nu,j,\sigma} \ll T$. In this weak coupling limit, a perturbation theory in the tunneling amplitude provides accurate results. Since we are not interested in the thermal excitations of the superconducting device, we additionally consider temperatures much smaller than the remaining energy scales. To compute the tunneling rates, we use the \mathcal{T} -matrix formalism, describing the transition probability between two states:

$$\Gamma_{i \rightarrow f} = 2\pi |\langle f | \mathcal{T} | i \rangle|^2 W_{if} \delta(E_i - E_f), \quad (7)$$

where W_{if} weights the rate through thermal distributions of the electrons in the leads, δ is the Dirac delta functional ensuring energy conservation between the initial and final states ($E_i = E_f$), and

$$\mathcal{T} = H_T + H_T \frac{1}{E_i - H_L - H_I + i0^+} \mathcal{T}, \quad (8)$$

which can be truncated at the desired order. In Eq. (7), and in the rest of the paper, we set $\hbar = 1$. The linear term in Eq. (8) describes the sequential tunneling; the higher order terms define, among other processes, the cotunneling contributions, which become progressively more important when the tunnel amplitudes t increase. In Appendix A we provide expressions for the sequential and the (second-order) cotunneling rates, used in this work to evaluate the transport through the superconducting islands.

The quantum state of the island is described by $|a\rangle = |N, N_C, \mathbf{n}\rangle$, where N_C is the number of Cooper pairs in the island and \mathbf{n} is a vector representing the occupation of the subgap and continuum excited states. The time derivative of the occupation probability of a given state is given by the master equation

$$\dot{P}_a = \sum_b [-\Gamma_{a \rightarrow b} P_a + \Gamma_{b \rightarrow a} P_b]. \quad (9)$$

Here we assume that coherences between different states in the superconducting island are negligible; indeed, we consider either model without near degeneracies where coherences cannot develop or with no coupling between degenerate states, due to different parity or spatial support. In the stationary limit, the system does not evolve in time and $\dot{P}_b^{\text{stat}} = 0$. These conditions, together with the normalization $\sum_b P_b^{\text{stat}} = 1$, form a linear system of equations for the occupation probabilities of the island states. Using the resulting stationary distribution, the current flowing from lead ν to the device is determined by the island transition rate to other states as

$$I_\nu = \sum_{a,b} \left[s \Gamma_{\nu,b \rightarrow a}^{\text{seq}} + \sum_{\nu' \neq \nu} \delta n(\nu) \Gamma_{\nu,\nu',b \rightarrow a}^{\text{cot}} \right] P_b^{\text{stat}}, \quad (10)$$

where we take $s = +1$ ($s = -1$) for electrons tunneling in (out) of the island and we set the electron charge to unity. Here $\delta n(\nu)$ is the net charge transferred from lead ν in a cotunneling process, and the sum runs over all the possible rates connecting the island state $|b\rangle$ with any state $|a\rangle$ (see Appendix A2 for more detail on the cotunneling rates Γ^{cot}).

In Eqs. (9) and (10) we are considering processes that change the island occupation by ± 1 electron, while neglecting local and crossed Andreev reflection processes [71]. This approximation is justified when the charging energy is the dominant energy scale, in particular $E_c \gg \Delta$, meaning that there is a large energy penalty for changing the charge of the device by $2e$. Throughout the rest of the paper we will indeed consider this strongly Coulomb-blockaded regime.

III. SINGLE NANOWIRE GEOMETRY

In this section we focus on resolving the spatial structure of subgap states in a single nanowire device coupled to two or three normal metallic leads. Regarding the spatial profile of the subgap state, we consider three situations: (i) a single subgap state delocalized at both ends of the nanowire but vanishing in its bulk, which we refer to as a ‘‘Majorana-like scenario,’’ (ii) two degenerate subgap states each localized close to one end of the device, and (iii) an extended subgap state that couples to all leads independently from their position. In all these cases we consider that the subgap states are strongly spin-split, behaving as effectively spinless. This situation can be achieved by a strong magnetic field or by proximity with ferromagnetic materials, and corresponds to standard models to achieve the topological regime [72]. Our goal is to distinguish between these possible scenarios based on the structure of the cotunneling steps and the nonlocal conductance.

A. Two-terminal device

We first focus on a two-terminal device, with leads coupled to the nanowire ends, which can host either a single subgap state or two degenerate ones located at the ends, see Figs. 2(a) and 2(b). For simplicity we choose a symmetric voltage drop at the contacts between the device and L and R leads by setting their chemical to $\mu_L = +V/2$ and $\mu_R = -V/2$, where V is the voltage bias.

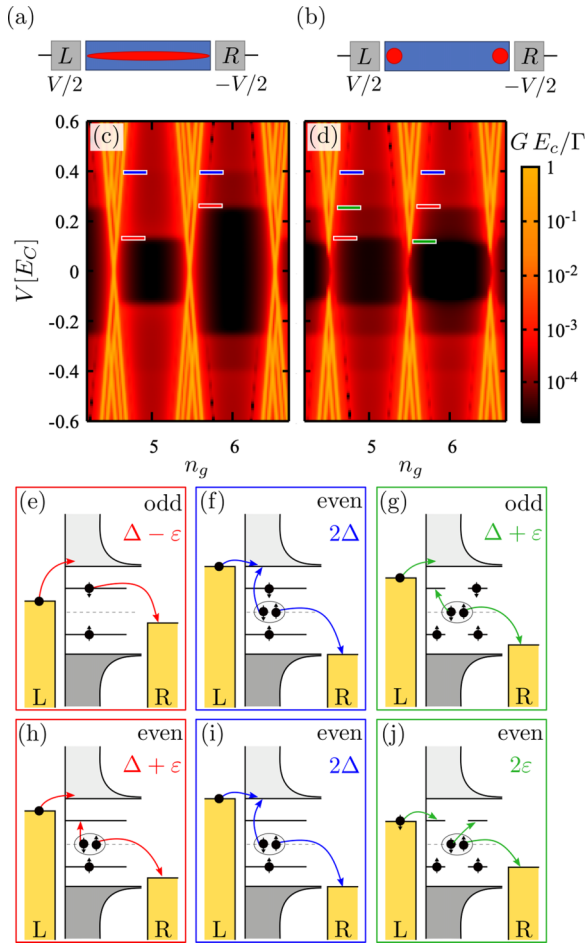


FIG. 2. Sketches of a nanowire coupled to two leads, hosting an extended (a) and two local states (b). (c) and (d) The differential conductance (in logscale) corresponding to cases (a) and (b), respectively, for subgap states with energies $\varepsilon = 0.3\Delta$. We show results for $\Delta = 0.2E_C$ and $\Gamma = 5 \times 10^{-5}E_C$. The color tics denote the dominant inelastic cotunneling processes, appearing at $V = 2\Delta$ (blue), $V = \Delta \pm \varepsilon$ for the even/odd Coulomb valley (red), and $V = 2\varepsilon$, $\Delta + \varepsilon$ (green). (e)–(j) Examples of the different cotunneling processes.

If the subgap levels have zero energy $\varepsilon = 0$, which is the case for ideal Majorana zero energy modes, the Coulomb-blockade structure is qualitatively similar in the two cases (data not shown). Instead, when $\varepsilon \neq 0$, the most evident difference is the strong reduction of the conductance peaks at $V = 0$ in the case of local states. This can be seen by comparing the conductance at $V \sim 0$ and half-integer n_g in Figs. 2(c) and 2(d). Indeed, when the subgap states do not couple to both leads, transport is suppressed at small biases because the subgap states cannot support resonant tunneling of electrons. This results in a much weaker conductance for $|V| < 2\varepsilon$, $\Delta - \varepsilon$ with respect to the situation where the subgap state connects both ends of the nanowire. However, zero-bias tunneling is still possible through elastic cotunneling, with an amplitude $\sim \Gamma_L \Gamma_R$ [71].

We also observe a clear difference in the structure of the cotunneling steps, highlighted by the colored tics in Figs. 2(c) and 2(d). In the case of an extended state, two inelastic cotunneling steps appear at $V = \Delta \pm \varepsilon$ for the even and the

odd valleys, corresponding to transitions to the lowest excited states (red tics) [60]. In the even valley it corresponds to the splitting of a Cooper pair, whose electrons end up in the subgap and the continuum of states. In the odd valley the lowest excitation corresponds to promoting the electron in the subgap state to the continuum. There are two additional steps due to the breaking of a Cooper pair into two electrons that enter the quasiparticle continuum (blue tics).

In the case with two states with local support, each coupled to a single lead, the number of cotunneling steps increases and, in particular, the threshold for inelastic cotunneling in the even-parity valleys decreases substantially. Indeed, the lowest excited state with even parity has an energy given by the sum of the energies of the two subgap states [see Fig. 2(j)]. In the case considered in the figure with the two states having the same energy, this threshold is 2ε . We note that this process does not require the creation of a quasiparticle excitation above the superconducting gap, reducing the conductance step onset with respect to the nondegenerate situation.

B. Three-terminal device

Next, we analyze a three terminal device, where two leads (L and R) couple to the nanowire ends and the third (M) probes the center of the device. Therefore, the M lead acts as a probe of the subgap support at the middle of the wire, distinguishing local and nonlocal states. The L and R leads are biased, with a chemical potential $\mu_L = +V/2$ and $\mu_R = -V/2$, respectively, while we consider that M is grounded ($\mu_M = 0$). The goal is to use the nonlocal conductance $G_M = \frac{dI_M}{dV}$ to detect whether the subgap state extends inside the device or is localized only on the edges. These two scenarios are sketched in Figs. 3(a) and 3(b). Furthermore, we explore the situations where the subgap states' energy ε is zero, Figs. 3(c) and 3(d), or finite, Figs. 3(e) and 3(f).

While the local conductance (through L and R) shows little dependence on the presence of a third lead and how it couples with the device (data not shown), the nonlocal conductance displays interesting features. First, notice that G_M is an odd function of the voltage bias V , thanks to the symmetry $R \leftrightarrow L$ we impose in our model: an inversion of the bias only changes the direction of the current flow between the L and R lead, while the current I_M remains insensitive to the sign of V since the lead is always grounded. Hence, the differential conductance ($G_M = \frac{dI_M}{dV}$) is an odd function of the voltage bias. When the lead does not couple to the subgap state, the conductance at $V = 0$ is suppressed, as clearly seen by comparing left and right panels in Fig. 3. Even though this effect is somehow trivial because low bias transport only involves the lowest energy level in a gapped system, its consequence is of great importance: The middle lead probes the density of states inside the wire. Hence, the M lead can resolve the spatial profile of subgap states and detect whether they have a nonvanishing projection on a specific portion of the device.

The nonlocal conductance also shows a peculiar sign dependence on n_g , illustrated by the sharp G_M jumps in Fig. 3. These sign changes appear whenever there is a crossing between ground states or excited states with different parities, corresponding to the crossing of the parabolas in Fig. 1(c) (see Appendix B for more details). Their dependence on V ,

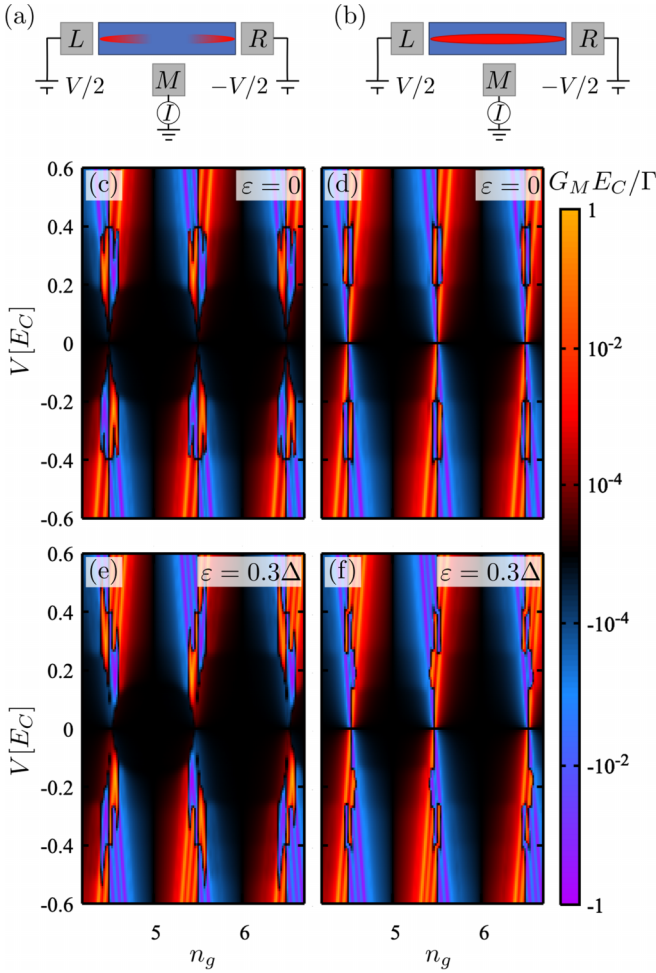


FIG. 3. Nonlocal differential conductance $G_M = \frac{dI_M}{dV}$ through a grounded lead coupled to the middle of the wire. (a) and (b) Situations where the middle lead does not and does couple to the subgap state (red blobs). (c) and (d) The nonlocal conductance for a case where the subgap state energy is $\varepsilon = 0$, while (e) and (f) show cases for $\varepsilon = 0.3\Delta$. (c) and (e) The subgap state structure shown in (a) while (d) and (f) correspond to (b). The remaining parameters are the same as in Fig. 2 and all the tunnel couplings are considered to be equal.

instead, arises from the necessity of having a chemical potential on the L and R leads large enough to populate the excited states coupled also with the M lead. This behavior can be better understood by considering the energy dependence of the superconducting island states on n_g and the sequential tunneling rates (see Appendix A 1 for their derivation). For instance, the rates describing the tunneling of an electron from the M lead to an empty quasiparticle state γ_j is $\Gamma_{M,i \rightarrow f} = \Gamma_M |u_j|^2 n_F(E_f - E_i)$, where i and f label the initial and final states with energy E_i and E_f . $\Gamma_M |u_j|^2$ is the effective tunneling rate in the wide-band limit multiplied by the local projector on the particlelike component of γ_j . Since the temperature is small, the Fermi factor n_F is a steplike function, activating the tunneling process mainly when $E_f - E_i < 0$. The opposite is true when we examine the process for extracting one electron from the occupied quasiparticle state γ_j , meaning that it is activated when $E_f - E_i > 0$. Hence, the sign of the

current in the M lead changes abruptly when n_g tunes the energy levels of the device across the resonance $E_i = E_f$, as adding/removing electrons from M becomes more favorable. We show more details in Fig. 5.

In conclusion, a three-terminal Coulomb-blockaded device has a highly tunable differential conductance alongside the standard transport suppression inside the Coulomb diamonds. As shown in Figs. 3(c)–3(f), this is a robust feature that requires neither the presence of a zero energy subgap state nor a third lead coupled only to the superconducting continuum, even though the latter is useful to have an extended bias window where the M lead is effectively decoupled from the device.

IV. DOUBLE NANOWIRE

In this section we extend the analysis of the nonlocal conductance to double nanowire setups; two parallel semiconductor nanowires are covered by the same floating superconducting island. The common superconductor allows the exchange of Cooper pairs between the wires, making them share a common charging energy, but it does not allow the tunneling of excitations above the gap from one wire to the other. In this context we therefore introduce two separate states at energy Δ to model the quasiparticle continua in the two wires. In contrast, we assume that subgap states can delocalize between the two wires. This setup for the device is inspired by recent experimental achievements [68,73–75] and the scope of exploring the topological Kondo effect when the system couples to more than two leads [64–66]. We consider that the nanowire ends couple to three different leads, as sketched in Figs. 4(a), 4(d), 4(g), and 4(j). As before, we consider that the L/R leads are symmetrically biased, while M is grounded. A different biasing condition is shown in Fig. 7 in Appendix B.

Regarding the spatial structure of subgap states, we identify four possible situations: ① two subgap states that extend along a single nanowire, ② a subgap state localized at each lead-device interface, ③ a common subgap state that couples with all three terminals, and ④ two subgap states localized respectively at the left and right ends of the double nanowire device. These scenarios are sketched in Figs. 4(a), 4(d), 4(g), and 4(j), while the panels below each sketch show the related local G_L and nonlocal G_M differential conductances. In all cases we consider degenerate subgap states with energy $\varepsilon = 0.3\Delta$. Subgap states with different energies would be easily detected by the different sizes of the Coulomb diamonds. The differences between the four cases are summarized in Table I.

Let us start from case ①, where each nanowire hosts a single subgap state with support on both ends. In this case there is no probe at the middle of any of the wires. Therefore, the transport features cannot distinguish between trivial extended states or nonlocal Majorana-like subgap states. The associated local conductance $G_L = \frac{dI_L}{dV}$, and the nonlocal one $G_M = \frac{dI_M}{dV}$, are reported in Figs. 4(b) and 4(c), respectively. Sequential tunneling processes contribute to the current between L and R at low bias, while they are suppressed for the M lead. A single sequential tunneling line is observed in G_L at low bias voltages; in the odd valleys, the stationary distribution P^{stat} has indeed a significant contribution from the configuration where a quasiparticle is frozen in the subgap state in the lower

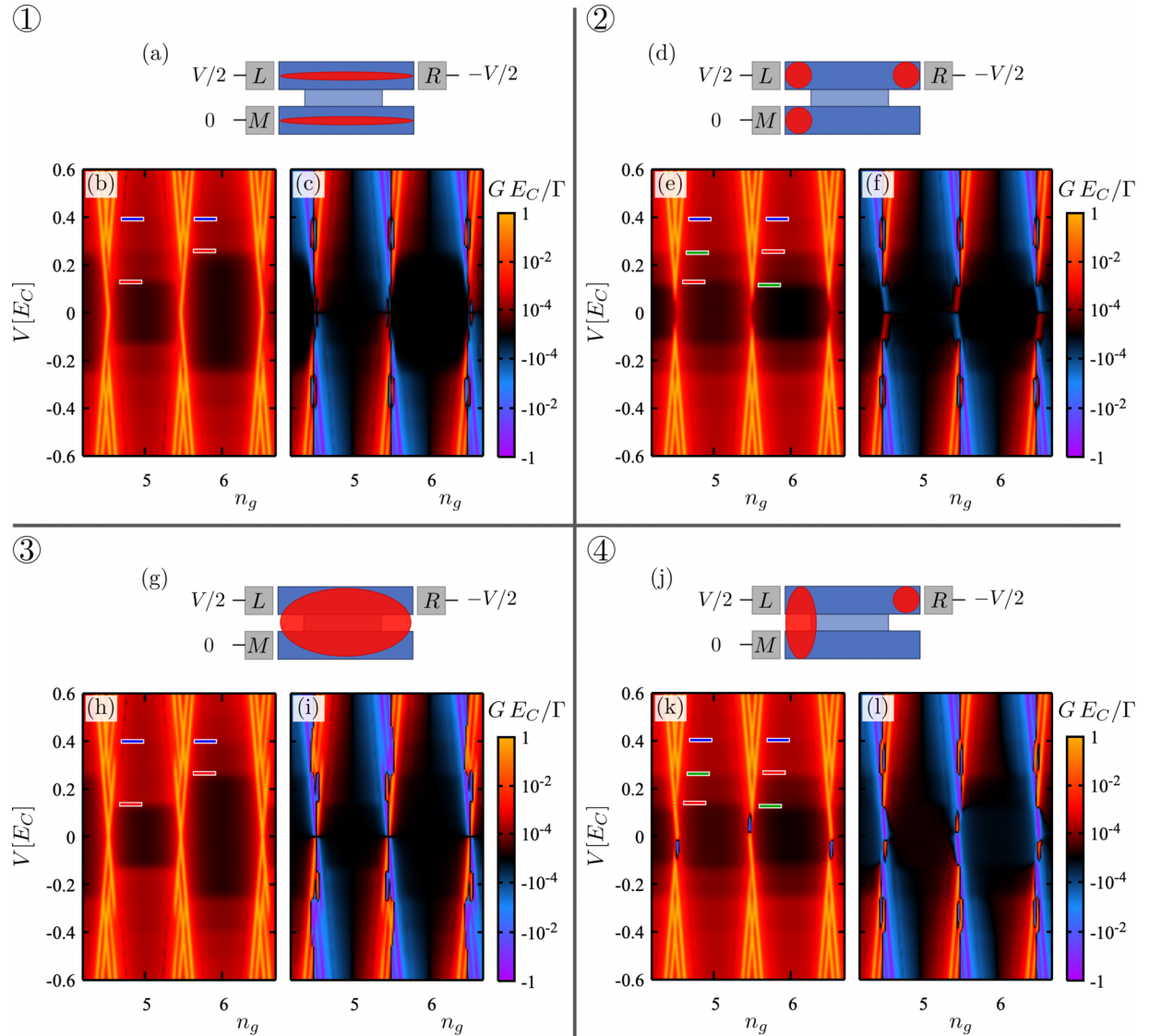


FIG. 4. Double wire system coupled via a trivial superconductor allowing the exchange of Cooper pairs, so the system has a common charging energy. ① One subgap state connects to L and R , while another couples to M (a). (b) and (c) The local conductance through the lead L and the nonlocal conductance through the grounded M lead, respectively. ② Situation for three local states coupled to the different leads, ③ an extended state coupled to all the leads, and ④ a local state that couples to R , while L and R couple to a different extended state. The parameters are the same as in Fig. 2.

wire. This is due to the imbalance between the Γ_M rates for incoming and outgoing particles at small temperatures. When the lower wire subgap state is occupied, the superconducting island cannot be excited by removing this quasiparticle via sequential tunneling through leads L or R , thus suppressing the leading-order transport mechanism in G_L . This is evident when comparing the odd valleys in Figs. 2(c) and 4(b): In proximity of the charge degeneracy points the sequential tunneling lines moving towards the odd valleys disappear and cotunneling becomes the dominating process at low bias. Also the weak conductance through the M lead at low bias voltage is due to cotunneling processes, where the device exchanges one electron with either L or R , and M , keeping the total charge on the superconducting island constant.

In case ②, when a trivial subgap state localizes at the interface with each lead, the conductance is suppressed for

$|V| < \varepsilon$. This is due to the local support of the subgap states, which cannot directly mediate sequential transport between different leads. Therefore, transport is dominated by elastic cotunneling at low bias voltages. The nonlocal conductance G_M , Fig. 4(f), displays feint resonances in the even valleys. The reason behind this is that tunneling processes between the superconducting island and the M lead involve (virtual) changes of the number of Cooper pairs in the island. The sign of the current depends on the charge difference between the ground and the lowest excited state.

Case ③ corresponds to a single subgap state coupled with all three leads. Therefore, the same Coulomb structure is present in the local and the nonlocal conductance, although the latter is an odd function of the bias V and exhibits sign changes when there are level crossings in the many-body spectrum of the superconducting device. The sequential

TABLE I. Summary of the main transport features for the four situations shown in Fig. 4.

① Sequential tunneling absent in G_M 2 cotunneling steps	② Sequential tunneling absent in all terminals 3 cotunneling steps
③ Sequential tunneling present in all terminals 2 cotunneling steps	④ Sequential tunneling absent in G_R 3 cotunneling steps Negative differential conductance in G_L

tunneling of electrons dominates transport, leading to strong conductance features at the charge degeneracy points for small bias voltages. Qualitatively, the signal of the M lead is equivalent to that shown in Fig. 3(f) for a single nanowire with an extended bound state.

The last possibility we analyze, case ④, corresponds to two degenerate subgap states, localized one in the left part and one in the right part of the device. This situation is of particular interest, as it might correspond to a double nanowire geometry where Majorana modes localized at each device ends strongly hybridize due to their small spatial separation. The local conductance G_L displays a parity dependent negative differential conductance (NDC) region at small bias, see Fig. 4(k). This is caused by a quasiparticle being trapped in the subgap state coupled to the R lead, blocking the current between the L and M leads. The appearance of the NDC region for either positive or negative bias is due to the electronlike or holelike excitation trapped in the right subgap state. In this regime, sequential transport through the right lead is suppressed, leading to a current reduction (not shown). For $|V| > 2\varepsilon$, the sequential transport channel to the right lead is open again, therefore making $|G_L| \neq |G_M|$. It also provides a relatively fast relaxation mechanism for the trapped quasiparticles in the right lead and the NDC region disappears.

The four cases show conductance steps inside the Coulomb valleys at finite voltage values. These steps appear when V matches the system excitation energy, opening the inelastic cotunneling channel: exchange of two electrons between the leads and the island, leaving it in an excited state (although keeping the island charge invariant). Depending on whether a bound state couples simultaneously to the L and R leads, cases ① and ③, or not, cases ② and ④, the number of cotunneling steps vary from 2 to 3 (colored tics in Fig. 4). A similar behavior has been described for the single wire situation, see discussion around Fig. 2.

Finally, we show in Appendix B another biasing situation, where L and M are symmetrically biased and R is grounded. We find that local and nonlocal transport can distinguish between the considered four situations also in that case.

V. CONCLUSIONS

In this paper we analyzed how the transport features of a multiterminal superconducting device with strong charging energy depend on the number and spatial structure of subgap bound states. In particular, we investigated the role of the spatial extent of the subgap states, which might not couple to all the leads attached to the device; we showed that the nonlocal differential conductance in multiterminal devices al-

lows for a qualitative characterization of their spatial profiles for biases below the superconducting gap. We considered a zero bandwidth model to describe the low-energy features of a superconducting floating island consisting of a proximitized single semiconducting nanowire or a pair of parallel nanowires. These systems are indeed known to host subgap states that determine the transport properties of the device. We focused on a situation where the charging energy E_C is the dominant energy scale, and we adopted a second-order master equations approach which allows us to characterize both the sequential tunneling of single electrons and the inelastic cotunneling events.

The sequential tunneling signal, dominating for small leads-device tunneling strength, gives information on the energy and spatial structure of the subgap states mediating transport. When two leads are not coupled by the lowest-energy states, the zero bias conductance is strongly suppressed, leaving only a faint cotunneling feature. In this way, transport can determine whether a state has support on the two ends of the wire. In the same way, additional leads can be added to gain spatial resolution inside the wire. Therefore, the absence of sequential tunneling conductance at low bias is a way to discriminate between trivial extended states and possible topological states with only support at the ends of the wires. Moreover, the number and voltage of inelastic cotunneling steps allow us to determine the number and the energies of the subgap states. The cotunneling signal is therefore another indicator that can be used to characterize the spatial structure of the subgap states. The described features hold for an arbitrary number of discrete subgap states with energy $|\varepsilon| > T, \Gamma$. For $\varepsilon < T, \Gamma$, instead, different subgap state configurations may result in the same qualitative transport features, thus hindering their spatial characterization.

Finally, electron transport in multiterminal Coulomb-blockaded devices results in an interesting pattern of peaks with positive and negative differential nonlocal conductance, depending on the induced charge n_g and on the voltage bias V . This allows us to switch the direction of the current flowing in the grounded lead, or suppress it, without changing the potential difference between the source and the drain but only by tuning the induced charge on the whole superconducting island.

We presented results based on a perturbative analysis of the transport properties, valid when the temperature is larger than the coupling between the leads and the device. Complementary methods are needed to describe the low-temperature and strong-coupling regimes, where electron correlations effects are important, in the nonequilibrium situation [76–78]. The master equation approach we presented, however, is less

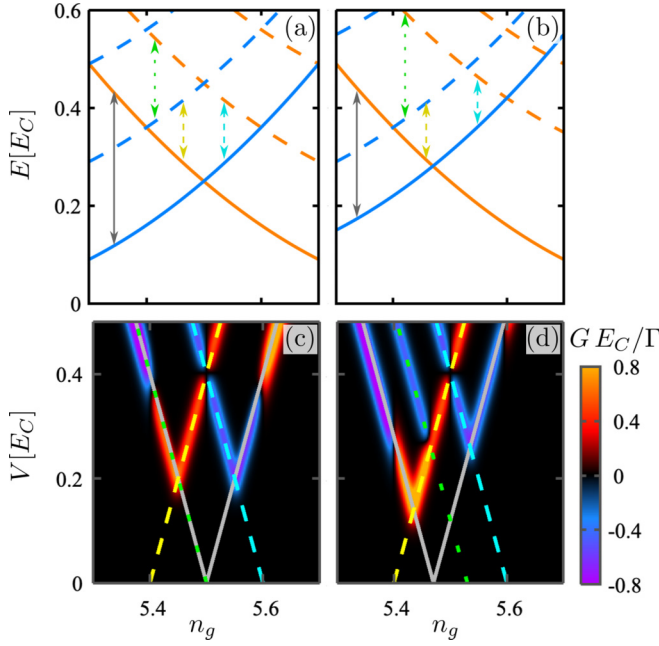


FIG. 5. (a) Many-body eigenenergies of the island for a spinless state at zero energy ($\Delta = 0.2E_C$). (b) Many-body energies for a subgap state at finite energy $\varepsilon = 0.3\Delta$. (c) Differential conductance through a middle lead that does not couple to the subgap state [see the sketch in Fig. 3(a)]. Here we consider only the sequential tunneling contribution to the current. (d) The corresponding results for $\varepsilon = 0.3\Delta$. The lines in the lower panels correspond to the excitation threshold denoted by the arrows in the upper ones. In (a) and (b) sequential tunneling via the M lead connects only states with different parity and charge occupation in the states at Δ . These processes always involve a relaxation from a higher energy state to a lower energy one, thus explaining the changes in sign of the differential conductance when two parabolas cross. The remaining parameters are the same as in Fig. 2.

computationally intensive and provides a clear picture of the transport mechanisms as long as nonperturbative effects can be neglected.

ACKNOWLEDGMENTS

We acknowledge support from the Danish National Research Foundation, the Danish Council for Independent Research | Natural Sciences, the European Research Council (Grant Agreement No. 856526), the Swedish Research Council, and NanoLund. M.M.W. and M.B. are supported by the Villum Foundation (Research Grant No. 25310). This project has received funding from the European Union's Horizon 2020 research and innovation program under the Marie Skłodowska-Curie grant agreement No. 847523 "INTERACTIONS."

APPENDIX A: TUNNELING RATES

1. Sequential tunneling rates

In this article we focus on the limit where the charging energy is the largest energy scale [$E_C \gg \max(|\Delta|, |V| \equiv |\mu_L - \mu_R|)$]. In this regime, transport is dominated by processes

where one electron is exchanged between the superconducting island and the leads. For Γ much smaller than any other energy scale, sequential tunneling processes yield the most prominent features in the conductance, providing the usual Coulomb diamond structure. The sequential rates are given by

$$\begin{aligned} \Gamma_{v,|N,N_C,\mathbf{n}\rangle \rightarrow |N+1,N_C,\mathbf{n}'\rangle}^{\text{seq}} &= \Gamma_v |u_j|^2 n_F(E_f - E_i - \mu_v), \\ \Gamma_{v,|N,N_C,\mathbf{n}\rangle \rightarrow |N-1,N_C,\mathbf{n}'\rangle}^{\text{seq}} &= \Gamma_v |u_j|^2 n_F(\mu_v + E_f - E_i), \\ \Gamma_{v,|N,N_C,\mathbf{n}\rangle \rightarrow |N+1,N_C+1,\mathbf{n}'\rangle}^{\text{seq}} &= \Gamma_v |v_j|^2 n_F(E_f - E_i - \mu_v), \\ \Gamma_{v,|N,N_C,\mathbf{n}\rangle \rightarrow |N-1,N_C-1,\mathbf{n}'\rangle}^{\text{seq}} &= \Gamma_v |v_j|^2 n_F(\mu_v + E_f - E_i), \end{aligned} \quad (\text{A1})$$

where n_F is the Fermi-Dirac distribution function and μ_v is the chemical potential of the lead $v = L, R, M$. Here we have used the wide-band approximation, where the tunneling rates are energy independent and $\Gamma_v = 2\pi \rho_F |t_v|^2$, with the lead density of states at the Fermi level ρ_F . These rates induce transitions between charge states differing by one electron, denoted through the vectors \mathbf{n} and \mathbf{n}' accounting for the fermionic occupation of the island states.

2. Cotunneling rates

Inside the Coulomb-blockaded region, inelastic cotunneling creates a series of steps in the differential conductance, where the voltage bias corresponds to energy differences between different states of the superconducting island. These are processes where one electron is transferred between two leads, leaving the island in an excited state. We also consider the elastic cotunneling that, instead, describes processes in which the island energy is conserved, and gives rise to the conductance background inside the diamond. However, we disregard local and crossed Andreev processes, where the island charge changes by $2e$, as they are suppressed by the strong charging energy in the system. The corresponding rates are given by Eq. (7), where

$$\begin{aligned} F_{v,v'}(\omega_1) &\equiv |\langle f | \mathcal{T} | i \rangle|^2 \\ &= \left| \sum_{m_1,v} \frac{\langle f | H_T(v) | m_1 \rangle \langle m_1 | H_T(v') | i \rangle}{E_{m_1} - E_i - \omega_1} \right. \\ &\quad \left. + \sum_{m_2,v} \frac{\langle f | H_T(v') | m_2 \rangle \langle m_2 | H_T(v) | i \rangle}{E_{m_2} - E_f + \omega_1} \right|^2. \end{aligned} \quad (\text{A2})$$

Here $H_T(v)$ describes the tunneling between the lead v and the island, v' denotes a lead different from v , and $m_{1,2}$ are virtual intermediate states. To derive this expression we have imposed energy conservation, which leads to a function dependent on the energy of the tunneling electron from/to one of the leads, ω_1 . The cotunneling rate can be written as

$$\begin{aligned} \Gamma_{v,v',i \rightarrow f}^{\text{cot}} &= 2\pi \int d\omega_1 F_{v,v'}(\omega_1) n_F(\omega_1 - \mu_L) \\ &\quad \times n_F(\mu_R + E_f - E_i - \omega_1). \end{aligned} \quad (\text{A3})$$

This expression for the cotunneling rates is divergent when the denominator in Eq. (A2) vanishes. To avoid the divergent behavior, we regularize the divergences as explained in Ref. [79]. The resulting integral can be formally solved

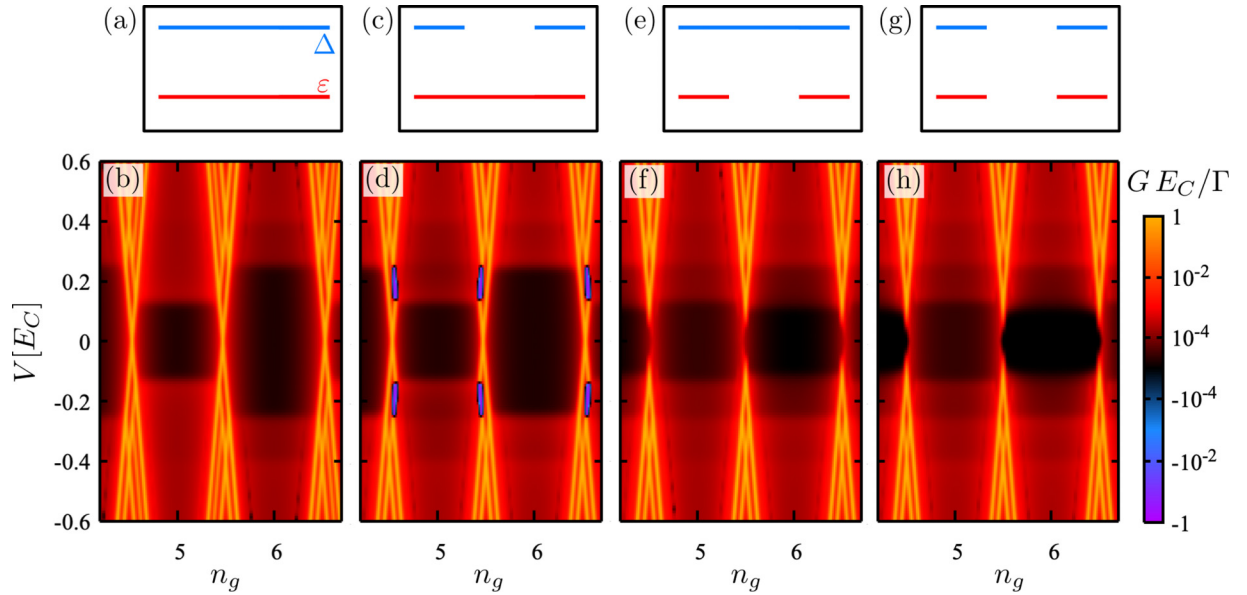


FIG. 6. Two-terminal conductance for different subgap and above gap states situations. (a) and (c) The situation where a bound state extends from left to right (red), while the state at higher energy can be either extended (a) or local (c). (b) and (d) The corresponding local conductance. (e) and (g) The situation where the island hosts local subgap states, whose corresponding conductance is shown in (f) and (h). Notice the NDC region appearing in (d): They correspond to a particle blocked in one of the two states at energy Δ and unable to tunnel out from the device on the other side, thus suppressing transport. Below the energy threshold required to populate the superconducting continuum ($|V| = 2\Delta$), transport is dominated by the properties of the subgap state alone: The low-bias peaks of (b) and (d) are almost identical and so are those of (f) and (h).

analytically [80], which leads to a complicated expression involving special functions. We find that for $T/E_C \gtrsim 10^{-3}$, it is computationally more efficient to expand the Fermi distribution function into a sum of complex Matsubara-Ozaki frequencies [81]

$$n_F(\omega - \mu) = \sum_{\alpha} r_{\alpha} \frac{1}{\omega - \mu + i\beta_{\alpha}}, \quad (\text{A4})$$

where β_{α} and r_{α} are the approximated Matsubara frequencies and residues, respectively. Finally, Eq. (A3) can be evaluated using the residue theorem, yielding to a rather compact expression

$$\Gamma_{v,v',i \rightarrow f}^{\text{cot}} = 8\pi \text{Im} \sum_{\alpha=0}^{\infty} r_{\alpha} \{n_F(\mu_R + E_f - E_i - \mu_L + i\beta_{\alpha}) \times [F_{v,v'}(\mu_L - i\beta_{\alpha}) - F_{v,v'}(\mu_R + E_f - E_i + i\beta_{\alpha})]\}. \quad (\text{A5})$$

This sum can be truncated at $\alpha \approx 100$ Matsubara-Ozaki frequencies for the parameters used in the calculations.

APPENDIX B: SUPPORTING RESULTS

In this Appendix we present additional results to support the chosen modeling of the considered devices and describe some details of the transport features presented in the main text. In particular, we first focus on the processes describing the transport of the three-terminal single-nanowire devices, which determine the transport across the lead M ; then we address the comparison between different modeling of the

quasiparticle states above the superconducting gap; finally, we consider a different choice of the voltage drop across the double-nanowire devices.

1. Features of the current across the lead M in the three-terminal nanowire

To understand the three-terminal transport features in a Coulomb-blockaded superconducting device, it is useful to compare the conductance dependence on the voltage bias and on the induced charge with the low-energy many-body spectrum. In Fig. 5 we report the eigenvalue structure and the nonlocal conductance $G_M = \frac{dI_M}{dV}$, close to the charge degeneracy point, for the device sketched in Fig. 3(a): A single Coulomb-blockaded nanowire hosting a subgap state that does not couple with the grounded lead M . The lowest energies of states with odd and even parity are represented by the continuous blue and orange lines, respectively, in Figs. 5(a) and 5(b). These states are connected via sequential tunneling involving a particle transfer to or from the subgap state, which does not contribute to the current flowing through the M lead. Hence G_M is suppressed at low bias, as can be seen in Figs. 5(c) and 5(d). The current in the M lead is activated only when V is large enough to populate excited states (via the L or the R leads) that can then relax to a lower energy state through a tunneling event between the superconducting continuum and the lead M . These processes correspond to transitions between a dashed line (i.e., states with excited quasiparticles in the superconducting continuum) and a continuous line with different parity (colors) in Figs. 5(a) and 5(b). These events are highlighted by the oblique lines in Figs. 5(c) and 5(d), representing energy thresholds for populating states that can

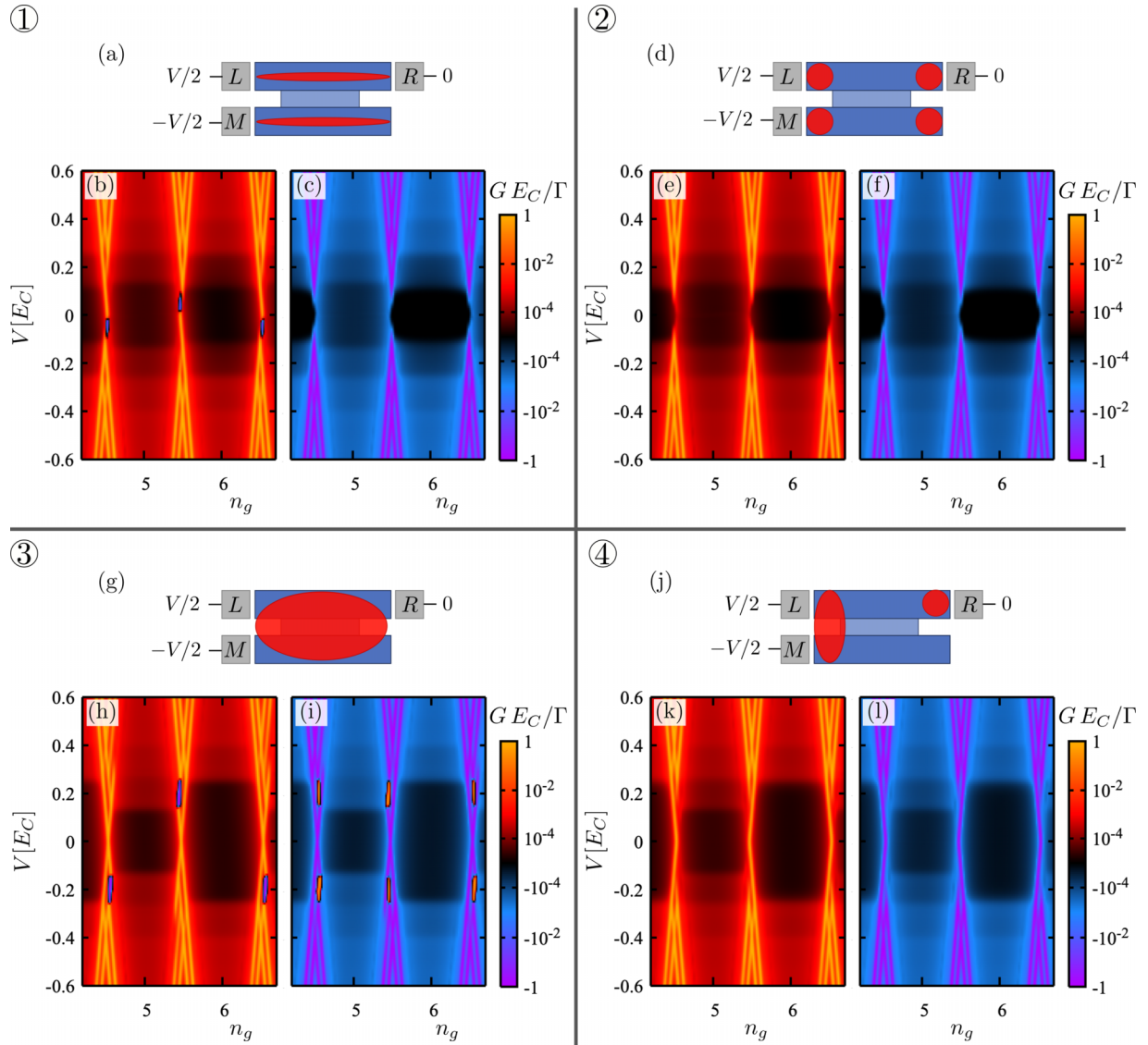


FIG. 7. Upper left panels: Sketch of the double wire system. ① One bound state connects L and R , while M connects to another one (a). (b) and (c) The conductance through the grounded M lead. ② Three local states coupled to the different leads. ③ An extended state coupled to all the leads. ④ A local state that couples to R , while L and R couple to another extended state. The parameters are the same as in Fig. 2. The conductance we show for lead M is $G_M = \frac{dI_M}{dV_R}$, hence it is always negative, with the exception of some small regions.

contribute to the current through M . The sign of the current, and hence of the conductance, changes at the crossing between energy levels with different parity. This phenomenology is independent from the energy ε of the subgap states, whether it is zero, as in Figs. 5(a) and 5(c), or finite, as in Figs. 5(b) and 5(d). The latter situation only has a slightly richer structure of the Coulomb diamonds due to the energy difference between the first excited states in the even and odd sectors.

Another interesting effect shown in Fig. 3 is the sign mismatch between the sequential tunneling and the cotunneling contribution close to the lower edge of the Coulomb diamonds. This can be seen at $V = \Delta$, where cotunneling (blurred signal) gives rise to negative conductance while sequential tunneling (sharp lines) contributes with positive conductance when n_g approaches 5.5 from below. Both can

be understood by considering the processes mediated by tunneling through the M lead for specific values of n_g and V . When $V > 0$ and $n_g \rightarrow 5.5$, the lowest energy excitation that can relax through the central lead is the odd parity state with a quasiparticle in the superconducting continuum that couples with an incoming electron to create a Cooper pair. This process is thus associated with a positive (ingoing) current from lead M . Instead, the lowest energy inelastic cotunneling step in the odd valley corresponds to the excitation of a quasiparticle from the subgap state to the continuum, mediated by the virtual occupation of the even parity state with no quasiparticle present. In this second-order process, the only tunneling event through the M lead is the destruction of a Cooper pair into the high-energy quasiparticle and an *outgoing* electron, which carries a negative particle current and, thus, negative conductance. Similar arguments explain the sign change

between sequential tunneling and cotunneling in other regions of the Coulomb diamonds.

2. One- vs two-state approximation to model the Bogoliubov quasiparticle continuum

Concerning the modeling of the quasiparticle continuum above the gap, in Fig. 6 we compare the two-terminal conductance for a nanowire with a single quasiparticle state at energy Δ coupled with both leads and with two degenerate quasiparticle states at the same energy with finite supports on each end, as sketched in the upper panels. The nanowire hosts one or two subgap states at energy ε . As long as the voltage bias is smaller than $\Delta - \varepsilon$, transport is dominated by the properties of the subgap state and the spatial structure of the superconducting continuum does not affect the qualitative features in conductance of the device. When the bias is larger and the states at energy Δ become accessible via sequential tunneling events, the “broken” continuum can trap a quasiparticle in one of the two edges of the device, suppressing transport and inducing a negative differential conductance region in the Coulomb diamonds. Notice, however, how this NDC is qualitatively different from that appearing in all data presented in the main

text, as it is a sequential tunneling feature appearing in the local conductance of two-terminal devices.

3. Example of the multiterminal transport with different voltage drops

Finally, in Fig. 7 we present the conductance results for the double nanowire geometry with a different bias choice with respect to the data shown in Fig. 4 in the main text: here we bias symmetrically leads L and M , while lead R is left grounded. The main difference with respect to Fig. 4 is that now the biased leads are not connected by a single superconducting continuum at energy Δ . In particular, notice the different natures of the NDC regions appearing in Figs. 7(b) and 7(h): In the former, it is due to a quasiparticle trapped in the subgap state connected to lead M and, indeed, it is not reflected in G_M . In the latter, it corresponds to a quasiparticle trapped in one of the two superconducting continua, in the upper or in the lower nanowire. This second case is similar to the data presented in Fig. 6(d), where the NDC is due to the broken superconducting continuum on a single nanowire, although the conductance in Fig. 7(h) is not symmetric in V because of the presence of the third terminal.

-
- [1] C. Janvier, L. Tosi, L. Bretheau, Ç. Ö. Girit, M. Stern, P. Bertet, P. Joyez, D. Vion, D. Esteve, M. F. Goffman, H. Pothier, and C. Urbina, Coherent manipulation of Andreev states in superconducting atomic contacts, *Science* **349**, 1199 (2015).
- [2] M. Hays, G. de Lange, K. Serniak, D. J. van Woerkom, D. Bouman, P. Krogstrup, J. Nygård, A. Geresdi, and M. H. Devoret, Direct Microwave Measurement of Andreev-Bound-State Dynamics in a Semiconductor-Nanowire Josephson Junction, *Phys. Rev. Lett.* **121**, 047001 (2018).
- [3] M. Hays, V. Fatemi, D. Bouman, J. Cerrillo, S. Diamond, K. Serniak, T. Connolly, P. Krogstrup, J. Nygård, A. L. Yeyati, A. Geresdi, and M. H. Devoret, Coherent manipulation of an Andreev spin qubit, *Science* **373**, 430 (2021).
- [4] E. Prada, P. San-Jose, M. W. A. de Moor, A. Geresdi, E. J. H. Lee, J. Klinovaja, D. Loss, J. Nygård, R. Aguado, and L. P. Kouwenhoven, From Andreev to Majorana bound states in hybrid superconductor–semiconductor nanowires, *Nat. Rev. Phys.* **2**, 575 (2020).
- [5] C. Nayak, S. H. Simon, A. Stern, M. Freedman, and S. Das Sarma, Non-Abelian anyons and topological quantum computation, *Rev. Mod. Phys.* **80**, 1083 (2008).
- [6] A. Y. Kitaev, Unpaired Majorana fermions in quantum wires, *Phys. Usp.* **44**, 131 (2001).
- [7] J. Alicea, New directions in the pursuit of Majorana fermions in solid state systems, *Rep. Prog. Phys.* **75**, 076501 (2012).
- [8] M. Leijnse and K. Flensberg, Introduction to topological superconductivity and Majorana fermions, *Semicon. Sci. Tech.* **27**, 124003 (2012).
- [9] C. W. J. Beenakker, Search for non-Abelian Majorana braiding statistics in superconductors, *SciPost Phys. Lect. Notes* **1**, 15 (2020).
- [10] R. Aguado, Majorana quasiparticles in condensed matter, *La Rivista del Nuovo Cimento* **40**, 523 (2017).
- [11] K. Sengupta, I. Žutić, H.-J. Kwon, V. M. Yakovenko, and S. Das Sarma, Midgap edge states and pairing symmetry of quasi-one-dimensional organic superconductors, *Phys. Rev. B* **63**, 144531 (2001).
- [12] K. T. Law, P. A. Lee, and T. K. Ng, Majorana Fermion Induced Resonant Andreev Reflection, *Phys. Rev. Lett.* **103**, 237001 (2009).
- [13] K. Flensberg, Tunneling characteristics of a chain of Majorana bound states, *Phys. Rev. B* **82**, 180516(R) (2010).
- [14] M. Wimmer, A. R. Akhmerov, J. P. Dahlhaus, and C. W. J. Beenakker, Quantum point contact as a probe of a topological superconductor, *New J. Phys.* **13**, 053016 (2011).
- [15] D. I. Pikulin, J. P. Dahlhaus, M. Wimmer, H. Schomerus, and C. W. J. Beenakker, A zero-voltage conductance peak from weak antilocalization in a Majorana nanowire, *New J. Phys.* **14**, 125011 (2012).
- [16] E. Prada, P. San-Jose, and R. Aguado, Transport spectroscopy of NS nanowire junctions with Majorana fermions, *Phys. Rev. B* **86**, 180503(R) (2012).
- [17] G. Kells, D. Meidan, and P. W. Brouwer, Near-zero-energy end states in topologically trivial spin-orbit coupled superconducting nanowires with a smooth confinement, *Phys. Rev. B* **86**, 100503(R) (2012).
- [18] C.-X. Liu, J. D. Sau, T. D. Stanescu, and S. Das Sarma, Andreev bound states versus Majorana bound states in quantum dot-nanowire-superconductor hybrid structures: Trivial versus topological zero-bias conductance peaks, *Phys. Rev. B* **96**, 075161 (2017).
- [19] C. Moore, C. Zeng, T. D. Stanescu, and S. Tewari, Quantized zero-bias conductance plateau in semiconductor-superconductor heterostructures without topological Majorana zero modes, *Phys. Rev. B* **98**, 155314 (2018).
- [20] A. Vuik, B. Nijholt, A. R. Akhmerov, and M. Wimmer, Reproducing topological properties with quasi-Majorana states, *SciPost Phys.* **7**, 061 (2019).

- [21] O. A. Awoga, J. Cayao, and A. M. Black-Schaffer, Supercurrent Detection of Topologically Trivial Zero-Energy States in Nanowire Junctions, *Phys. Rev. Lett.* **123**, 117001 (2019).
- [22] H. Pan and S. Das Sarma, Physical mechanisms for zero-bias conductance peaks in Majorana nanowires, *Phys. Rev. Res.* **2**, 013377 (2020).
- [23] J. Avila, F. Peñaranda, E. Prada, P. San-Jose, and R. Aguado, Non-Hermitian topology as a unifying framework for the Andreev versus Majorana states controversy, *Commun. Phys.* **2**, 133 (2019).
- [24] J. Cayao and P. Buset, Confinement-induced zero-bias peaks in conventional superconductor hybrids, *Phys. Rev. B* **104**, 134507 (2021).
- [25] T. O. Rosdahl, A. Vuik, M. Kjaergaard, and A. R. Akhmerov, Andreev rectifier: A nonlocal conductance signature of topological phase transitions, *Phys. Rev. B* **97**, 045421 (2018).
- [26] J. Danon, A. B. Hellenes, E. B. Hansen, L. Casparis, A. P. Higginbotham, and K. Flensberg, Nonlocal Conductance Spectroscopy of Andreev Bound States: Symmetry Relations and BCS Charges, *Phys. Rev. Lett.* **124**, 036801 (2020).
- [27] R. Hess, H. F. Legg, D. Loss, and J. Klinovaja, Local and nonlocal quantum transport due to Andreev bound states in finite Rashba nanowires with superconducting and normal sections, *Phys. Rev. B* **104**, 075405 (2021).
- [28] A. Melo, C.-X. Liu, P. Rožek, T. Örn Rosdahl, and M. Wimmer, Conductance asymmetries in mesoscopic superconducting devices due to finite bias, *SciPost Phys.* **10**, 037 (2021).
- [29] D. I. Pikulin, B. van Heck, T. Karzig, E. A. Martinez, B. Nijholt, T. Laeven, G. W. Winkler, J. D. Watson, S. Heedt, M. Temurhan, V. Svidenko, R. M. Lutchyn, M. Thomas, G. de Lange, L. Casparis, and C. Nayak, Protocol to identify a topological superconducting phase in a three-terminal device, [arXiv:2103.12217](https://arxiv.org/abs/2103.12217).
- [30] R. Singh and B. Muralidharan, Conductance spectroscopy of Majorana zero modes in superconductor-magnetic insulating nanowire hybrid systems, [arXiv:2203.08413](https://arxiv.org/abs/2203.08413).
- [31] A. Maiani, M. Geier, and K. Flensberg, Conductance-matrix symmetries of multiterminal semiconductor-superconductor devices, *Phys. Rev. B* **106**, 104516 (2022).
- [32] A. Tsintzis, R. Seoane Souto, and M. Leijnse, Creating and detecting poor man's Majorana bound states in interacting quantum dots, *Phys. Rev. B* **106**, L201404 (2022).
- [33] J. Gramich, A. Baumgartner, and C. Schönenberger, Andreev bound states probed in three-terminal quantum dots, *Phys. Rev. B* **96**, 195418 (2017).
- [34] G. C. Ménard, G. L. R. Anselmetti, E. A. Martinez, D. Puglia, F. K. Malinowski, J. S. Lee, S. Choi, M. Pendharkar, C. J. Palmstrøm, K. Flensberg, C. M. Marcus, L. Casparis, and A. P. Higginbotham, Conductance-Matrix Symmetries of a Three-Terminal Hybrid Device, *Phys. Rev. Lett.* **124**, 036802 (2020).
- [35] D. Puglia, E. A. Martinez, G. C. Ménard, A. Pöschl, S. Gronin, G. C. Gardner, R. Kallaher, M. J. Manfra, C. M. Marcus, A. P. Higginbotham, and L. Casparis, Closing of the induced gap in a hybrid superconductor-semiconductor nanowire, *Phys. Rev. B* **103**, 235201 (2021).
- [36] E. A. Martinez, A. Pöschl, E. B. Hansen, M. A. Y. van de Poll, S. Vaitiekėnas, A. P. Higginbotham, and L. Casparis, Measurement circuit effects in three-terminal electrical transport measurements, [arXiv:2104.02671](https://arxiv.org/abs/2104.02671).
- [37] G. Wang, T. Dvir, N. van Loo, G. P. Mazur, S. Gazibegovic, G. Badawy, E. P. A. M. Bakkers, L. P. Kouwenhoven, and G. de Lange, Nonlocal measurement of quasiparticle distribution in proximitized semiconductor nanowires using quantum dots, *Phys. Rev. B* **106**, 064503 (2022).
- [38] T. Dvir, G. Wang, N. van Loo, C.-X. Liu, G. P. Mazur, A. Bordin, S. L. D. ten Haaf, J.-Y. Wang, D. van Driel, F. Zatelli, X. Li, F. K. Malinowski, S. Gazibegovic, G. Badawy, E. P. A. M. Bakkers, M. Wimmer, and L. P. Kouwenhoven, Realization of a minimal Kitaev chain in coupled quantum dots, [arXiv:2206.08045](https://arxiv.org/abs/2206.08045).
- [39] A. Pöschl, A. Danilenko, D. Sabonis, K. Kristjuhan, T. Lindemann, C. Thomas, M. J. Manfra, and C. M. Marcus, Nonlocal signatures of hybridization between quantum dot and Andreev bound states, *Phys. Rev. B* **106**, L161301 (2022).
- [40] A. Pöschl, A. Danilenko, D. Sabonis, K. Kristjuhan, T. Lindemann, C. Thomas, M. J. Manfra, and C. M. Marcus, Nonlocal conductance spectroscopy of Andreev bound states in gate-defined InAs/Al nanowires, *Phys. Rev. B* **106**, L241301 (2022).
- [41] A. Banerjee, O. Lesser, M. A. Rahman, C. Thomas, T. Wang, M. J. Manfra, E. Berg, Y. Oreg, A. Stern, and C. M. Marcus, Local and nonlocal transport spectroscopy in planar Josephson junctions, [arXiv:2205.09419](https://arxiv.org/abs/2205.09419).
- [42] M. Aghaee *et al.*, InAs-Al hybrid devices passing the topological gap protocol, [arXiv:2207.02472](https://arxiv.org/abs/2207.02472).
- [43] B. van Heck, A. R. Akhmerov, F. Hassler, M. Burrello, and C. W. J. Beenakker, Coulomb-assisted braiding of Majorana fermions in a Josephson junction array, *New J. Phys.* **14**, 035019 (2012).
- [44] B. M. Terhal, F. Hassler, and D. P. DiVincenzo, From Majorana Fermions to Topological Order, *Phys. Rev. Lett.* **108**, 260504 (2012).
- [45] T. Hyart, B. van Heck, I. C. Fulga, M. Burrello, A. R. Akhmerov, and C. W. J. Beenakker, Flux-controlled quantum computation with Majorana fermions, *Phys. Rev. B* **88**, 035121 (2013).
- [46] S. Plugge, L. A. Landau, E. Sela, A. Altland, K. Flensberg, and R. Egger, Roadmap to Majorana surface codes, *Phys. Rev. B* **94**, 174514 (2016).
- [47] D. Aasen, M. Hell, R. V. Mishmash, A. Higginbotham, J. Danon, M. Leijnse, T. S. Jespersen, J. A. Folk, C. M. Marcus, K. Flensberg, and J. Alicea, Milestones Toward Majorana-Based Quantum Computing, *Phys. Rev. X* **6**, 031016 (2016).
- [48] L. A. Landau, S. Plugge, E. Sela, A. Altland, S. M. Albrecht, and R. Egger, Towards Realistic Implementations of a Majorana Surface Code, *Phys. Rev. Lett.* **116**, 050501 (2016).
- [49] S. Plugge, A. Rasmussen, R. Egger, and K. Flensberg, Majorana box qubits, *New J. Phys.* **19**, 012001 (2017).
- [50] T. Karzig, C. Knapp, R. M. Lutchyn, P. Bonderson, M. B. Hastings, C. Nayak, J. Alicea, K. Flensberg, S. Plugge, Y. Oreg, C. M. Marcus, and M. H. Freedman, Scalable designs for quasiparticle-poisoning-protected topological quantum computation with Majorana zero modes, *Phys. Rev. B* **95**, 235305 (2017).
- [51] J. Manousakis, C. Wille, A. Altland, R. Egger, K. Flensberg, and F. Hassler, Weak Measurement Protocols for Majorana Bound State Identification, *Phys. Rev. Lett.* **124**, 096801 (2020).

- [52] M. Nitsch, R. Seoane Souto, and M. Leijnse, Interference and parity blockade in transport through a Majorana box, *Phys. Rev. B* **106**, L201305 (2022).
- [53] R. S. Souto and M. Leijnse, Fusion rules in a Majorana single-charge transistor, *SciPost Phys.* **12**, 161 (2022).
- [54] A. P. Higginbotham, S. M. Albrecht, G. Kiršanskas, W. Chang, F. Kuemmeth, P. Krogstrup, T. S. Jespersen, J. Nygård, K. Flensberg, and C. M. Marcus, Parity lifetime of bound states in a proximitized semiconductor nanowire, *Nat. Phys.* **11**, 1017 (2015).
- [55] S. M. Albrecht, E. B. Hansen, A. P. Higginbotham, F. Kuemmeth, T. S. Jespersen, J. Nygård, P. Krogstrup, J. Danon, K. Flensberg, and C. M. Marcus, Transport Signatures of Quasiparticle Poisoning in a Majorana Island, *Phys. Rev. Lett.* **118**, 137701 (2017).
- [56] S. M. Albrecht, A. P. Higginbotham, M. Madsen, F. Kuemmeth, T. S. Jespersen, J. Nygård, P. Krogstrup, and C. M. Marcus, Exponential protection of zero modes in Majorana islands, *Nature (London)* **531**, 206 (2016).
- [57] E. C. T. O'Farrell, A. C. C. Drachmann, M. Hell, A. Fornieri, A. M. Whiticar, E. B. Hansen, S. Gronin, G. C. Gardner, C. Thomas, M. J. Manfra, K. Flensberg, C. M. Marcus, and F. Nichele, Hybridization of Subgap States in One-Dimensional Superconductor-Semiconductor Coulomb Islands, *Phys. Rev. Lett.* **121**, 256803 (2018).
- [58] E. B. Hansen, J. Danon, and K. Flensberg, Probing electron-hole components of subgap states in Coulomb blockaded Majorana islands, *Phys. Rev. B* **97**, 041411(R) (2018).
- [59] S. Vaitiekėnas, G. W. Winkler, B. van Heck, T. Karzig, M.-T. Deng, K. Flensberg, L. I. Glazman, C. Nayak, P. Krogstrup, R. M. Lutchyn, and C. M. Marcus, Flux-induced topological superconductivity in full-shell nanowires, *Science* **367**, eaav3392 (2020).
- [60] S. Vaitiekėnas, R. S. Souto, Y. Liu, P. Krogstrup, K. Flensberg, M. Leijnse, and C. M. Marcus, Evidence for spin-polarized bound states in semiconductor–superconductor–ferromagnetic-insulator islands, *Phys. Rev. B* **105**, L041304 (2022).
- [61] A. M. Whiticar, A. Fornieri, E. C. T. O'Farrell, A. C. C. Drachmann, T. Wang, C. Thomas, S. Gronin, R. Kallaher, G. C. Gardner, M. J. Manfra, C. M. Marcus, and F. Nichele, Coherent transport through a Majorana island in an Aharonov-Bohm interferometer, *Nat. Commun.* **11**, 3212 (2020).
- [62] D. Razmadze, D. Sabonis, F. K. Malinowski, G. C. Ménard, S. Pauka, H. Nguyen, D. M. T. van Zanten, E. C. T. O'Farrell, J. Suter, P. Krogstrup, F. Kuemmeth, and C. M. Marcus, Radio-Frequency Methods for Majorana-Based Quantum Devices: Fast Charge Sensing and Phase-Diagram Mapping, *Phys. Rev. Appl.* **11**, 064011 (2019).
- [63] D. Sabonis, E. C. T. O'Farrell, D. Razmadze, D. M. T. van Zanten, J. Suter, P. Krogstrup, and C. M. Marcus, Dispersive sensing in hybrid InAs/Al nanowires, *Appl. Phys. Lett.* **115**, 102601 (2019).
- [64] B. Béri and N. R. Cooper, Topological Kondo Effect with Majorana Fermions, *Phys. Rev. Lett.* **109**, 156803 (2012).
- [65] A. Altland, B. Béri, R. Egger, and A. M. Tsvelik, Multichannel Kondo Impurity Dynamics in a Majorana Device, *Phys. Rev. Lett.* **113**, 076401 (2014).
- [66] A. Zazunov, A. Altland, and R. Egger, Transport properties of the Coulomb–Majorana junction, *New J. Phys.* **16**, 015010 (2014).
- [67] T. Kanne, D. Olsteins, M. Marnauza, A. Vekris, J. C. Estrada Saldaña, S. Loric, R. D. Schlosser, D. Ross, S. Csonka, K. Grove-Rasmussen, and J. Nygård, Double nanowires for hybrid quantum devices, *Adv. Funct. Mater.* **32**, 2107926 (2022).
- [68] A. Vekris, J. C. Estrada Saldaña, T. Kanne, T. Hvid-Olsen, M. Marnauza, D. Olsteins, M. M. Wauters, M. Burrello, J. Nygård, and K. Grove-Rasmussen, Electronic transport in double-nanowire superconducting islands with multiple terminals, *Nano Lett.* **22**, 5765 (2022).
- [69] J. Ekström, P. Recher, and T. L. Schmidt, Transport properties of coupled Majorana bound states in the Coulomb blockade regime, *Phys. Rev. B* **101**, 195420 (2020).
- [70] R. A. Žak and K. Flensberg, Coulomb blockade of a three-terminal quantum dot, *Phys. Rev. B* **77**, 045329 (2008).
- [71] B. van Heck, R. M. Lutchyn, and L. I. Glazman, Conductance of a proximitized nanowire in the Coulomb blockade regime, *Phys. Rev. B* **93**, 235431 (2016).
- [72] R. M. Lutchyn, E. P. A. M. Bakkers, L. P. Kouwenhoven, P. Krogstrup, C. M. Marcus, and Y. Oreg, Majorana zero modes in superconductor–semiconductor heterostructures, *Nat. Rev. Mater.* **3**, 52 (2018).
- [73] O. Kürtösy, Z. Scherübl, G. Fülöp, I. E. Lukács, T. Kanne, J. Nygård, P. Makk, and S. Csonka, Andreev molecule in parallel InAs nanowires, *Nano Lett.* **21**, 7929 (2021).
- [74] A. Vekris, J. C. E. Saldaña, T. Kanne, M. Marnauza, D. Olsteins, F. Fan, X. Li, T. Hvid-Olsen, X. Qiu, H. Xu, J. Nygård, and K. Grove-Rasmussen, Josephson junctions in double nanowires bridged by *in-situ* deposited superconductors, *Phys. Rev. Res.* **3**, 033240 (2021).
- [75] A. Vekris, J. C. Estrada Saldaña, J. de Bruijkere, S. Lorić, T. Kanne, M. Marnauza, D. Olsteins, J. Nygård, and K. Grove-Rasmussen, Asymmetric Little–Parks oscillations in full shell double nanowires, *Sci. Rep.* **11**, 19034 (2021).
- [76] P. Schmitteckert, Nonequilibrium electron transport using the density matrix renormalization group method, *Phys. Rev. B* **70**, 121302(R) (2004).
- [77] R. Seoane Souto, A. E. Feiguin, A. Martín-Rodero, and A. L. Yeyati, Transient dynamics of a magnetic impurity coupled to superconducting electrodes: Exact numerics versus perturbation theory, *Phys. Rev. B* **104**, 214506 (2021).
- [78] C.-M. Chung, M. M. Wauters, and M. Burrello, Matrix product state simulations of quantum quenches and transport in Coulomb blockaded superconducting devices, *Phys. Rev. B* **106**, 094308 (2022).
- [79] S. Koller, M. Grifoni, M. Leijnse, and M. R. Wegewijs, Density-operator approaches to transport through interacting quantum dots: Simplifications in fourth-order perturbation theory, *Phys. Rev. B* **82**, 235307 (2010).
- [80] J. Koch, F. von Oppen, Y. Oreg, and E. Sela, Thermopower of single-molecule devices, *Phys. Rev. B* **70**, 195107 (2004).
- [81] T. Ozaki, Continued fraction representation of the Fermi-Dirac function for large-scale electronic structure calculations, *Phys. Rev. B* **75**, 035123 (2007).